Engineering 34 (2024) 164–173

Contents lists available at ScienceDirect

Engineering

journal homepage: www.elsevier.com/locate/eng

Research
Material Science and Engineering—Article

Rational Design of and Mechanism Insight into an Efficient Antifreeze Peptide for Cryopreservation

Haishan Qi [a,#], Yihang Gao [a,#], Lin Zhang [a], Zhongxin Cui [a], Xiaojie Sui [a], Jianfan Ma [a], Jing Yang [a], Zhiquan Shu [b], Lei Zhang [a,*]

[a] Department of Biochemical Engineering, School of Chemical Engineering and Technology, Frontier Science Center for Synthetic Biology and Key Laboratory of Systems Bioengineering (MOE), Tianjin University, Tianjin 300350, China
[b] School of Engineering and Technology, University of Washington Tacoma, Tacoma, WA 98402, USA

ARTICLE INFO

Article history:
Received 23 November 2022
Revised 11 January 2023
Accepted 31 January 2023
Available online 1 June 2023

Keywords:
Antifreeze peptides
Evolution analysis
Ice recrystallization inhibition
Molecular dynamics simulation
Cryopreservation
Synthetic biology

ABSTRACT

The development of effective antifreeze peptides to control ice growth has attracted a significant amount of attention yet still remains a great challenge. Here, we propose a novel design method based on in-depth investigation of repetitive motifs in various ice-binding proteins (IBPs) with evolution analysis. In this way, several peptides with notable antifreeze activity were developed. In particular, a designed antifreeze peptide named AVD exhibits ideal ice recrystallization inhibition (IRI), solubility, and biocompatibility, making it suitable for use as a cryoprotective agent (CPA). A mutation analysis and molecular dynamics (MD) simulations indicated that the Thr6 and Asn8 residues of the AVD peptide are fundamental to its ice-binding capacity, while the Ser18 residue can synergistically enhance their interaction with ice, revealing the antifreeze mechanism of AVD. Furthermore, to evaluate the cryoprotection potential of AVD, the peptide was successfully employed for the cryopreservation of various cells, which demonstrated significant post-freezing cell recovery. This work opens up a new avenue for designing antifreeze materials and provides peptide-based functional modules for synthetic biology.

© 2024 THE AUTHORS. Published by Elsevier LTD on behalf of Chinese Academy of Engineering and Higher Education Press Limited Company. This is an open access article under the CC BY-NC-ND license (http://creativecommons.org/licenses/by-nc-nd/4.0/).

1. Introduction

The formation and growth of ice crystals inside cells are extremely harmful to living biological systems, leading to lethal mechanical and chemical injuries at the cellular level. In nature, ice-binding proteins (IBPs) produced by psychrotolerant organisms can bind to ice crystals and control the crystals' growth, thereby endowing their hosts with the capacity to survive in subzero conditions [1,2]. However, the high immunogenicity, instability, and cost of IBPs limit their applications [3]. Inspired by IBPs, mimics such as polymers, peptides, macromolecules, and two-dimensional (2D) materials have been developed [4,5]. Antifreeze peptides have been proposed and have attracted widespread attention due to their low immunogenicity and effective antifreeze activity [1]. Thus far, the structure–function relationships of IBPs are not completely clear, and the rational design of antifreeze peptides is still difficult and challenging. Current strategies for obtaining antifreeze peptides include directed evolution from mutagenesis, enzymatic hydrolysis of food-borne proteins, and simple structural mimics of IBPs [3,6].

Repetitive motifs are sequence repetitions that occur in 14% of proteins across all domains of life [7]; they are thought to originate from replication slippage and recombination events of genomes [8,9]. Many natural IBPs contain repetitive motifs, which can generate arrays and form ice-binding surfaces (IBSs) to match the ice lattice; this endows the IBPs with the macroscopic properties of ice recrystallization inhibition (IRI) and thermal hysteresis (TH) [10,11]. Moreover, conservative residue regions in many proteins are usually functionally important and even essential, as they provide fitness advantages from positive Darwinian selection over millions of years [12]. This information has been demonstrated and employed to guide enzyme-directed evolution and functional module design in synthetic biology [13–16]. As IBPs have undergone positive selection to adapt to subzero environments [17], it is feasible to use the conservative information on the amino acid sequence and structure of IBPs to guide the mining and design of antifreeze modules.

* Corresponding author.
E-mail address: lei_zhang@tju.edu.cn (L. Zhang).
# These authors contributed equally to this work.

https://doi.org/10.1016/j.eng.2023.01.015
2095-8099/© 2024 THE AUTHORS. Published by Elsevier LTD on behalf of Chinese Academy of Engineering and Higher Education Press Limited Company.
This is an open access article under the CC BY-NC-ND license (http://creativecommons.org/licenses/by-nc-nd/4.0/).

In this study, a novel strategy is proposed to rationally design antifreeze peptides based on repetitive motifs. A total of 233 IBPs with regular structures from 22 psychrotolerant species were systematically classified and an evolution analysis was carried out. Then, the HHrepID and MEME programs were jointly employed to define the repetitive motifs in the classified IBPs. In addition, a conservative analysis was performed to develop antifreeze peptides using the WebLogo algorithm. Several peptides with antifreeze properties were designed. In particular, an antifreeze peptide denoted as AVD, derived from *Marinomonas primoryensis* IBPs (*Mp*IBPs), was obtained that displays optimal IRI activity and solubility. The structure of AVD was determined by means of circular dichroism (CD) spectra and model simulations. Mutational analysis and molecular dynamics (MD) simulations further indicated the critical residues for the ice binding and antifreeze mechanism of AVD. Finally, the biocompatibility and cell membrane stabilization function were investigated, and AVD was employed for cell cryopreservation. This strategy sheds light on the design of novel antifreeze peptides.

2. Materials and methods

2.1. Materials

Sequences of IBPs from divergent psychrotolerant organisms were collected from the GenBank and UniProt databases. The NIH-3T3, RAW264.7, and GLC-82 cell lines were purchased from the cell bank of the type culture collection of the Chinese Academy of Sciences (Shanghai, China). All peptides were obatined from GL Biochem (Shanghai, China). Trypan blue stain solution, Fura-2, and adenosine triphosphate (ATP) assay kit were acquired from Solarbio (Beijing, China). Fluorescein isothiocyanate (FITC) monomers were obtained from Shanghai Macklin Biochemical Co., Ltd. (China), and Tubulin-Tracker Red was purchased from Beyotime Biotechnology (Shanghai, China). RNAiso Plus, PrimeScript RT reagent Kit, and SYBR Premix Ex Taq were obtained from TaKaRa (Dalian, China). Dulbecco's modified Eagle's medium (DMEM), RPMI-1640, and fetal bovine serum were purchased from Gibco (Grand Island, NY, USA).

2.2. Phylogenetic analyses

To construct the phylogenetic tree, we collected the sequences of IBPs from the beetles ($n = 25$), *Choristoneura fumiferana* ($n = 7$), *Lolium perenne* ($n = 5$), *Marinomonas primoryensis* ($n = 4$), *Daucus carota* ($n = 3$), and *Deschampsia antarctica* ($n = 7$) from the GenBank and UniProt databases. First, these amino acid sequences were aligned using Clustal X. Then, the model WAG + F + G was chosen as the model of best fit according to the Bayesian information criterion. We performed the maximum likelihood (ML) phylogenetic tree with a bootstrap of 1000 replications to assess node support by means of IQ-tree. In addition, Bayesian phylogenetic analyses were performed using MrBayes v.3.2.6. Ten million generations were run and sampled every 1000 generations. Then, 10 000 phylogenetic trees were obtained and 25% of these were discarded as burn-in.

2.3. Detection of IRI activities

The IRI activities of the peptides were detected via optical microscopy on a cooling stage. First, 20 μL of solution was dropped from a height of 1 m onto a thin aluminum block placed on liquid nitrogen, forming a glass slide. Then, the sample was placed on the cooling stage at −60 °C and kept for 1 min. After that, the sample was heated to −9 °C at 5 °C·min^{-1} and annealed at −9 °C for 30 min. Photographs were taken every 5 min during the annealing process. NIS-Elements D imaging software was employed to measure the mean grain areas (MGAs) of the ice crystals. Five regions were randomly selected, and all the ice crystal areas in these regions were measured. Three experimental runs were performed for every sample, and the results were employed to calculate the mean area using Prism 5.0.

2.4. Circular dichroism measurements

CD measurements were performed using a J-810 spectropolarimeter (Jasco, Germany). The peptides were dissolved in phosphate-buffered saline (PBS) with a final concentration of 1 mg·mL^{-1}. Then, they were placed in a 0.1 mm path length quartz cuvette. Their adsorption was tested in the far ultraviolet (UV) spectral range of 190–260 nm at 25, 15, and 4 °C. The Reed model was employed to analyze the distribution of the peptide secondary structures.

2.5. Models

The structure of AVD was obtained through homology modeling using the structure of the *Mp*IBP (Protein Data Bank (PDB) ID: 3P4G) as a template. Then, the structure of AVD was used as the initial conformation, and four independent MD simulations were run for 100 ns. In this way, 4000 models were obtained. During the MD simulations, the CHARMM36 force field was used. Water was represented using the TIP4P/Ice model. The temperature was set as 230 K for the formation of ice. Ramachandran plots were built with the statistics of dihedral angles along the simulation trajectories.

2.6. Molecular dynamics simulations

A simulation system with or without AVD solvated in the water was performed, employing the all-atomistic CHARMM36 force field. The TIP4P/Ice water model was used for the MD simulations, as it is suitable for the simulation of biomolecules coming into contact with ice [18]. GROMACS 5.1.4 was used. The simulation box had the dimensions of 9 nm × 5 nm × 9 nm. The box without AVD contained 3696 ice crystals and 9891 water molecules. For the system with AVD, 1 AVD molecule was put into the equilibrated ice/water box in the vicinity of the ice, resulting in a box containing 1 AVD molecule, 3696 ice crystals, 9891 water molecules, and four Na^+ ions as counter ions. Before the MD simulation was carried out, energy minimization was performed for 10 000 steps, with the steepest descent algorithm where the ice was fixed. Next, five independent simulations were run; each was 50 ns long at 230 K. Periodic boundary conditions (PBCs) were applied in three dimensions, and the integration time-step for the Verlet algorithm was set to 2 fs. The cutoff for the van der Waals and electrostatic interactions was set to 1.2 nm. All bonds were constrained using the LINCS algorithm. All data were collected every 5 ns. The interaction between the AVD peptide and ice during the ice formation process was analyzed by means of Pymol 2.3.4. To determine whether a certain water molecule belonged to an ice crystal or to the supercooled liquid phase, we employed a strategy based on the F_4 order-parameter and angular order parameter (AOP)/F_3 parameter.

2.7. Dynamic ice shaping

The morphologies of the ice shapes and the ice growth rates were observed using a homemade Nanoliter osmometer and were recorded with a camera (Nikon Y-TV55, Japan). In brief, a six-well sample holder coated with silicon oil on one side was put onto a

thermal control stage. Then, a sub-microliter volume of peptide solution was injected into the sample holder using a microsyringe. After that, the sample was quickly frozen at a cooling rate of 0.35 °C·s^{-1} from room temperature to −20 °C to form an ice slurry; this was followed by quickly melting at a rate of 0.35 °C·s^{-1} until many small ice grains were observed. At that time, the melting rate was changed from 0.35 to 0.01 °C·s^{-1}, and the small ice grains continued to melt until a single ice crystal was obtained. The melting point (T_m) was recorded when the formed single ice crystal no longer melted. After that, the sample was cooled to a desired point with a cooling rate of 0.01 °C·s^{-1}, and the ice growth process was recorded with a camera. ImageJ was used to measure the growth rate, which was calculated according to the elongation of the diameter (Δd) of the ice crystal within the desired time (Δt). Three independent experiments were repeated for each sample in this study.

2.8. Cell cryopreservation and recovery assays

All kinds of cells were incubated at 37 °C under 5% CO_2 in a CO_2 incubator. Before the experiments, the cells were trypsinized and counted using a hemocytometer (Sigma-Aldrich, USA). The cell density was adjusted to 2×10^5 cells per milliliter. Then, 1 mL of cells was put into a centrifuge tube and centrifuged at 800 r·min^{-1} for 5 min. The supernatant was removed and resuspended with 1 mL of the cryoprotective agent (CPA) in a cryovial (Corning, USA). The CPAs were prepared as follows: Different concentrations of the AVD or AVD-3 peptides were mixed with 2%, 3%, or 1% dimethyl sulfoxide (DMSO) in DMEM, in which the solubility of AVD and AVD-3 could reach 10 mg·mL^{-1}. After that, the cryovials were transferred into a cell-freezing container (BeyoCool™ FCFC012, Beyotime Biotechnology). Then, they were stored at −80 °C for 24 h.

For cell recovery, the cryopreserved samples were thawed at 37 °C until all the ice was melted. The cells were then centrifuged at 800 r·min^{-1} for 5 min. The supernatant was discarded and the cell pellet was resuspended in 1 mL of fresh cell media. Then, the samples were transferred to a 24-well plate and maintained in a humidified atmosphere of 5% CO_2 at 37 °C for 24 h of incubation. The cell suspension was used for the trypan blue exclusion assay [19]. The cells were stained with 0.04% trypan blue and counted using a hemocytometer. Cell recovery was calculated as

$$\text{Cell recovery} = \frac{N_{\text{after}}}{N_{\text{before}}} \times 100\%$$

where N_{after} is the number of live cells after cryopreservation and N_{before} is the total number of live cells before cryopreservation.

2.9. Cell proliferation

The post-thawed cells were plated in a 96-well plate at a density of 200 cells per well. Cell viability was investigated with an ATP assay kit (Solarbio) every 24 h.

2.10. Determination of tubulin configuration

The post-thawed cells were put into a dish and cultured for 24 h. Then, they were fixed with 4% paraformaldehyde for 15 min. After that, Tubulin-Tracker Red was incubated with the cells for 45 min to mark the tubulin, and Hoechst 33342 was incubated with the cells for 5 min to track the nucleus. Each step was followed by three washes with PBS containing 0.5% Triton-100 (5 min each). Fluorescence imaging was performed by means of a confocal microscope (Nikon, Japan).

2.11. Statistical analysis

The data were expressed as the mean ± standard error of the mean (SEM). The statistical analysis was performed using two-tailed Student's unpaired *t*-tests. GraphPad Prism 5.0 was used for the analysis and graphs. All experiments were performed in triplicate.

3. Results and discussion

3.1. Evolution analysis of IBPs with repetitive motifs

IBPs with different structures undergo convergent evolution under the strong life-or-death selective pressure provided by sub-zero temperatures. For example, many IBPs contain a flat and hydrophobic IBS, which is formed by repetitive structural loops [20]. In these loops, critical amino acid residues that participate in binding ice crystals tend to be arrayed in identical orientations, resulting in a consensus motif [20–23]. During the long adaptive process, the beneficial mutations of IBPs conferred the host with a functional advantage while increasing the probability of the host being retained in the population. Therefore, IBPs with more conservative sequences usually have greater antifreeze ability [12]. In this work, inspired by IBPs, antifreeze peptides were designed by analyzing the regular loops and optimizing the residues in the IBPs through evolution analysis (Fig. 1(a)). First, the structure landscapes of IBPs with regular loops were collected based on the PDB database (Fig. S1 in Appendix A). The *Deschampsia antarctica* IBP was considered because it is highly homologous to the *Lolium perenne* IBP. Similarly, the IBPs from *Dendroides canadensis*, *Microdera dzhungarica punctipennis*, and *Anatolica polita* were also employed due to their high homologies with the *Tenebrio molitors* IBPs [24]. Thus, a total of 233 IBPs from 22 different psychrotolerant species were sorted for subsequent analysis (Table S2 in Appendix A).

Sequence–structure–function relations reveal that regular structures commonly consist of repetitive primary sequences. However, the primary sequences of a portion of IBPs may not be conserved despite their structures are regular, which is attributed to the exchange, insertion, and deletion of amino acid residues in IBPs during long-term evolution. Therefore, the HHrepID program, a automated procedure for the *de novo* identification of repeats in proteins, was employed to investigate the IBPs [25–27]. In Fig. S2 in Appendix A, the duplicated regions of the IBP sequences are represented by dark diagonal lines and circled in red. In this way, 51 sequences from nine species with repetitive sequences were selected, including *Tenebrio molitors* ($n = 14$), *Dendroides canadensis* ($n = 5$), *Microdera dzhungarica punctipennis* ($n = 4$), and *Anatolica polita* ($n = 2$) (together referred to as "beetles"); and *Choristoneura fumiferana* ($n = 7$), *Lolium perenne* ($n = 5$), *Marinomonas primoryensis* ($n = 4$), *Deschampsia antarctica* ($n = 7$), and *Daucus carota* ($n = 3$) (Fig. S2).

Many hosts of IBPs inhabit in sea-ice environments, which are regarded as "hot spots" for horizontal gene transfer (HGT) [28]. Thus, certain IBPs may be highly homologous despite their remote phylogeny [29]. For example, two isoforms derived from *Antarctomyces psychrotrophicus* share low sequence identity, because they independently evolved from different bacteria via HGT [29]. Therefore, a phylogenetic tree was employed to depict the evolutionary distances of the 51 sequences described above that possessed repetitive primary sequences (Fig. 1(b); Fig. S3 in Appendix A). The topologies of the Bayesian and ML trees are almost congruent with each other. As can be seen in Fig. 1(b) and Fig. S3, the isoforms belonging to the same species almost share a common subclade, indicating that they originated from the same ancestor. More specifically, the beetle IBPs and the *Choristoneura fumiferana* IBPs (*Cf*IBPs) are nested within one subfamily containing two subclades,

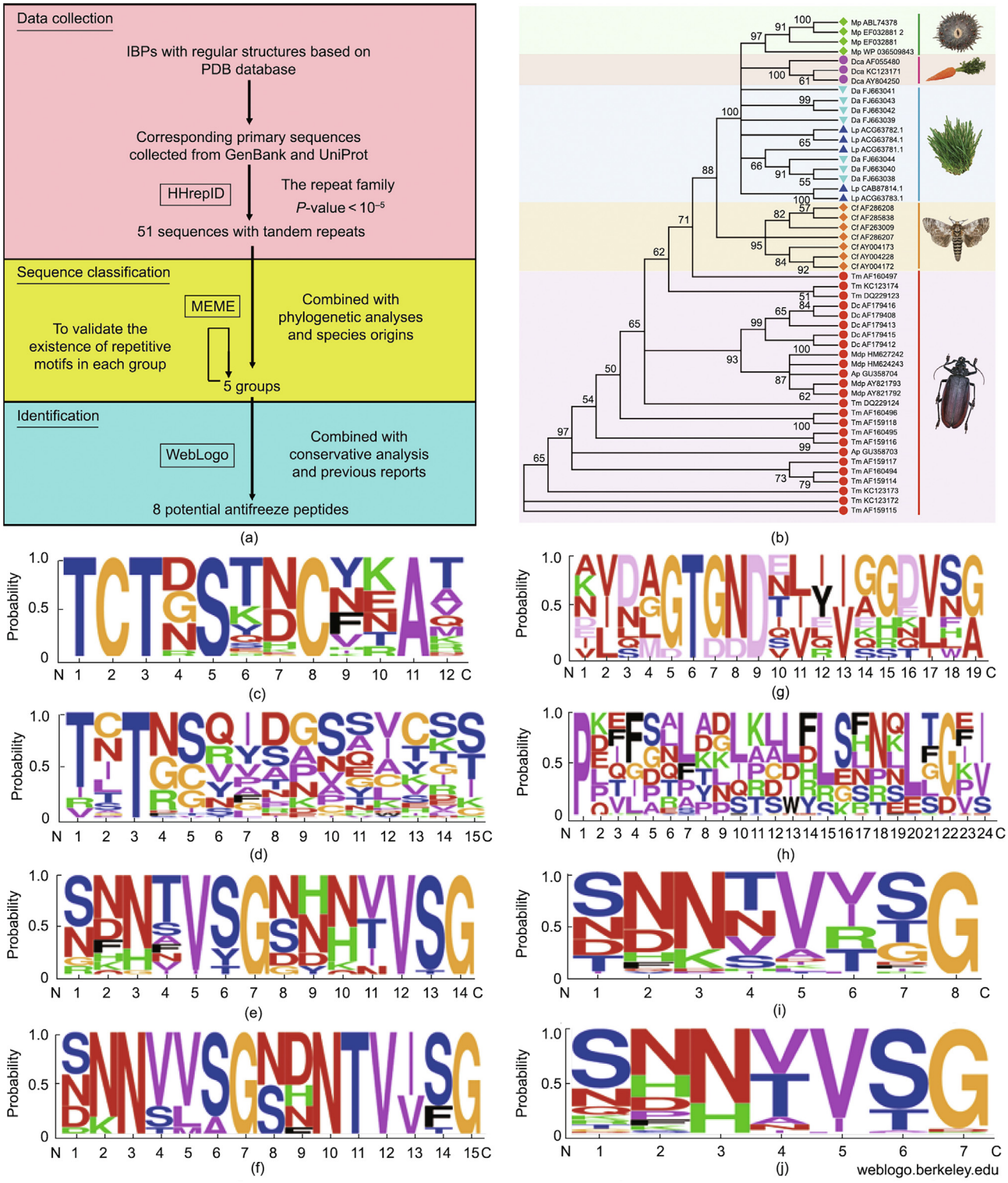

Fig. 1. Design of antifreeze peptides. (a) Flow chart for designing novel antifreeze peptides. (b) Phylogenetic tree of IBPs from nine psychrotolerant organisms obtained via ML analysis. (c–j) Conservative analysis of repetitive amino acid sequences from their motifs.

indicating their close evolutionary distances (Fig. 1(b)). In addition, the IBPs from *Lolium perenne* and *Deschampsia antarctica* share a common subclade, reflecting their high homologies. The *Daucus carota* IBPs (*Dca*IBPs) and *Mp*IBPs are all nested within their respective subfamilies, and their distant phylogenetic relationships manifest the diversity of molecular origins.

Thus, these sequences were classified into five groups (Fig. 1(b)). The MEME program, an unsupervised learning algorithm for searching motifs in protein sequences, was employed to further analyze the repetitive motifs. As shown in Fig. S4 in Appendix A, all groups display repetitive motifs, indicating that the classification is reliable [30]. Selection and conservative analysis of the repetitive motifs were also carried out (Figs. 1(c)–(j)). As shown in Figs. S5–S9 in Appendix A, the repetitive motifs contain ice-binding sites, and the critical residues participate in stabilizing the protein structures. Based on a comprehensive analysis of the

conservative and nonconservative residues in the motifs, eight peptides were designed (Figs. 1(c)–(j); Table S3 in Appendix A).

3.2. IRI performance of the peptides

The designed peptides were synthesized by means of solid-phase synthesis protocols. Mass spectrometry (MS) and high-performance liquid chromatography (HPLC) data of designed peptides are provided in Figs. S10–S17 in Appendix A. The peptides' solubility was also measured and is presented in Table S4 in Appendix A. Among these peptides, TCT, TCTN, and AVD were soluble in PBS, and their IRI properties were further tested. First, the time tracing of ice grain areas was performed (Fig. 2(a)). During the annealing time, a proportion of the ice grains continued to increase, while other smaller ones generally melted and disappeared due to Oswald ripening, which can reduce the surface free energy of the whole system. Compared with the PBS control, the ice grain recrystallization was significantly suppressed in the TCT, TCTN, and AVD samples. After being annealed for 30 min, the MGAs of the TCT, TCTN, and AVD samples were 74.7%, 65.7%, and 14.1% relative to the PBS control (Fig. 2(b)). The IRI performance of these peptides was further investigated at different concentrations. As shown in Fig. S18 in Appendix A, the IRI activities of these peptides are concentration dependent.

A hydrophilic zwitterionic motif containing alternating positively charged lysine (K) and negatively charged glutamic acid (E) was fused to the C-terminal of the SNNT, SNNV, PKE, SNNVV, and SNNTV peptides to improve their solubility. MS and HPLC data for these peptides are provided in Figs. S19–S23 in Appendix A.

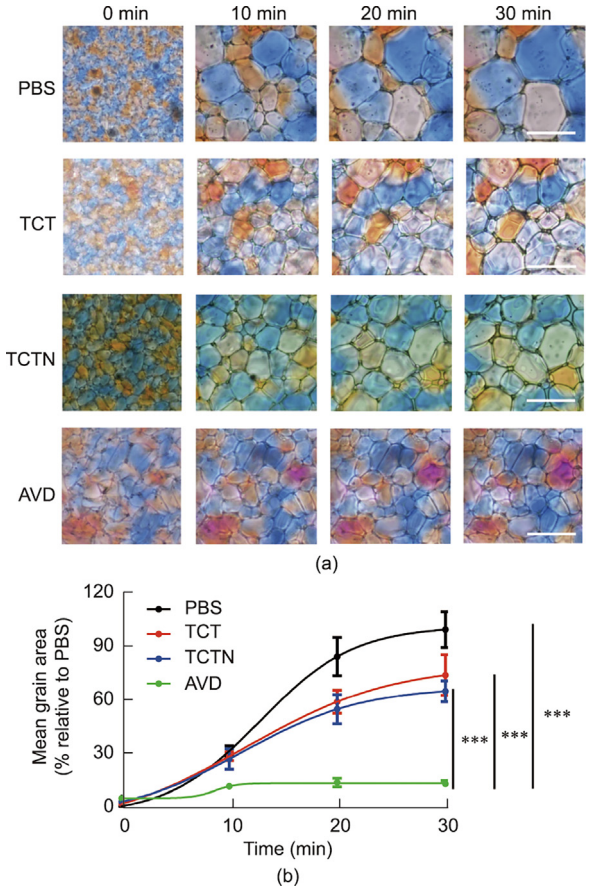

Fig. 2. IRI activities of peptides. (a) Cryomicrographs of ice crystals grown in the presence of 5 mg·mL^{-1} of TCT, TCTN, or AVD peptides (scale bar: 100 μm). (b) Time-traced MGAs of recrystallizing ice domains from different solutions (results presented as mean ± SEM; ***$p < 0.001$).

The SNNT, PKE, and SNNVV peptides could be dissolved in PBS after EKylation and exhibited IRI activities (Fig. S24 in Appendix A). Their MGAs were 52%, 44%, and 43% relative to the PBS at 1 mg·mL^{-1}, displaying weaker IRI activity than AVD. Besides, a comparison of the antifreeze abilities of AVD and other reported antifreeze peptides is provided in Table S5 in Appendix A, which shows that AVD exhibited the top-ranking IRI activity. AVD was also compared with typical antifreeze materials in a dose response (Fig. S25 in Appendix A). In comparison with PVA56 [31] and PC-AFP$_{22}$ monomer [32], AVD showed higher IRI activity. When compared with the cyclic ice-binding peptide (peptide 8), AVD and peptide 8 displayed individual characters. AVD possessed higher IRI activity at low concentrations (< 0.5 mg·mL^{-1}), while peptide 8 exhibited an advantage at high concentrations. Graphene oxide also displayed excellent IRI activity similar to that of PVA [33].

The antifreeze abilities of the AVD peptide and its original protein *Mp*IBP were further compared. Both displayed excellent IRI activity (Table S6 in Appendix A). The ice crystals in the AVD solutions grew in a stepwise manner, mostly in the direction of the *a*-axes, similar to that in *Mp*IBP solutions. However, the growth pattern in the AVD solution was much smoother and slower, which is conducive to cell cryopreservation. Therefore, considering its solubility and antifreeze activities, AVD was selected to be studied in more detail.

3.3. Structure of the AVD peptide

CD was employed to investigate the secondary structures of AVD at temperatures ranging from 4 to 25 °C in the far UV spectral range (190–260 nm wavelength). As shown in Figs. 3(a) and (b), the β-sheet percentage was 56.1% at 25 °C, 56.1% at 15 °C, and 55.2% at 4 °C. These results indicated that the secondary structure of AVD was stable at different temperatures. MD simulations were also employed to determine the three-dimensional (3D) model of the AVD peptide. The peptide's initial conformation was modeled using *Mp*IBP (PDB entry: 3P4G) as a template, and the structure was equilibrated for 100 ns. The obtained conformations were then sorted based on their distribution probabilities in Ramachandran plots. The Ramachandran plots of the AVD peptide at 298 K are shown in Fig. 3(c). The plots represent the distribution probabilities as a function of the dihedral angles between amino acids. The β-sheet conformation was the dominant secondary structure at 69.2%, which is consistent with the CD results and the structure of the root protein *Mp*IBP [22]. This experiment and the results of the MD simulation indicated that the AVD peptide is mainly composed of β-sheet elements.

The model with the highest scores calculated by the Ramachandran plots was selected and is presented in Fig. 3(d). The spatial conformation revealed a spacing of 7.8 Å between the oxygen atoms of the Thr6 and Asn8 side chains, which can match the spacing of oxygen atoms on the primary prism plane and the basal plane of ice crystals [20,34]. The relative distribution probabilities and the AVD structures with the 10 highest scores are summarized in Fig. S26 in Appendix A, with spacing distances varying from 4.2 to 12.0 Å. The root-mean-square deviation (RMSD) values, which are presented in Fig. S27 in Appendix A, indicated that AVD was well equilibrated during the simulations.

3.4. Mutation analysis and MD simulations of AVD antifreeze activity

The molecular-level details of the interaction between the AVD peptide and ice crystals were investigated by means of site-directed mutation and MD simulations. The spacing between the Thr6 and Asn8 residues in AVD is similar to the ice lattice distance between the basal and prism planes of ice crystals (Fig. 3(d)).

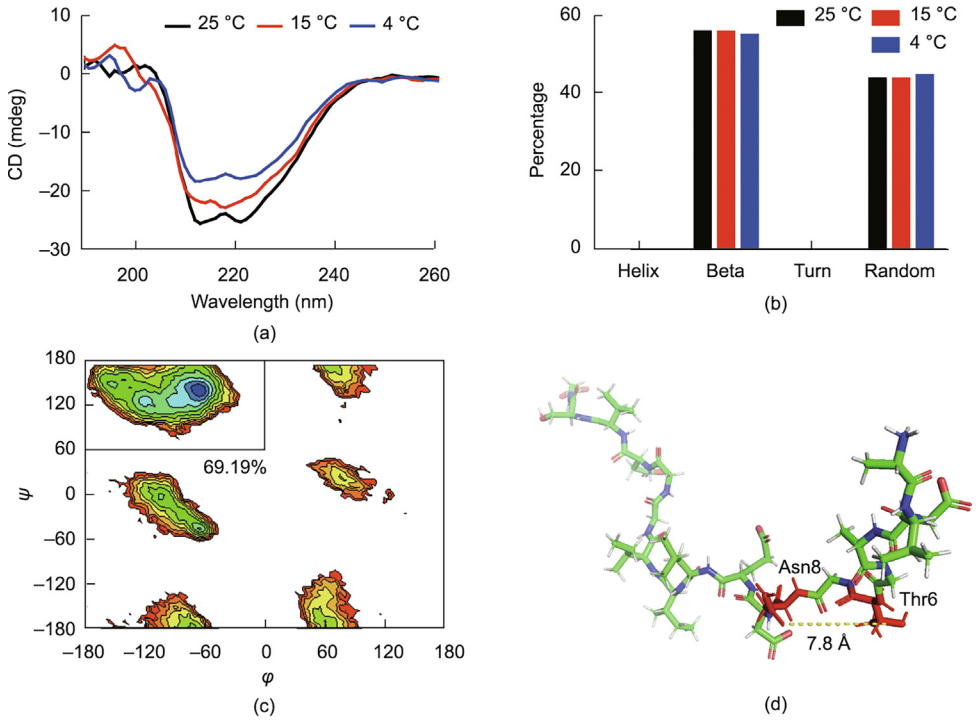

Fig. 3. Structure of the AVD peptide. (a) CD spectra at 25, 15, and 4 °C. (b) Secondary structure distribution. (c) Ramachandran plots at 25 °C. (d) 3D structure of AVD; the threonine residue and aspartic acid residue are highlighted in red, while other residues are highlighted in green. The distance between Thr6 and Asn8 is shown as a yellow dashed line.

Therefore, we hypothesize that this AVD location can act as a putative ice-binding site. Furthermore, as the methyl group of the ice-binding site on AVD plays an important role in maintaining conformational rigidity and immobilizing the water molecules [35], we selected Ser as an alternative amino acid which does not have methyl groups [36]. Thus, three mutant peptides were prepared with Thr6, Asn8, or both being replaced by Ser (Fig. 4(a)). MS and HPLC data of these peptides are provided in Figs. S28–S30 in Appendix A. The dynamic ice shaping and IRI activities of the three mutant peptides were then evaluated (Figs. 4(b)–(e)). The mutants displayed higher ice growth rates and significantly reduced IRI activity, indicating that the Thr6 and Asn8 residues are essential in arresting ice growth.

The interaction mechanism between the AVD peptide and ice crystals was analyzed by means of MD simulations. Four independent simulations were performed for each sample, with each simulation being run at 220 K. The AVD peptide was placed in a random orientation situated in the vicinity of a growing ice front at the start of the simulations. As shown in Figs. 4(f) and (g), the AVD peptide significantly inhibited the formation of ice crystals in the simulation. At 40 ns in the group without AVD, the ice growth entered a plateau stage and made up about 85% of the whole system, whereas the ice made up about 59% at 40 ns in the AVD group. Snapshots of the AVD peptide binding to the ice were taken at 40 ns during Trajectory 2 from two perspectives, as illustrated in Fig. 4(h). These snapshots revealed that the Thr6 and Asn8 residues were shoved into a cavity in the ice surface. These results further confirmed the important role of the Thr6 and Asn8 residues in the binding of AVD to ice. Interestingly, we also found that the carbonyl of Ser18 had interactions with the ice crystals via hydrogen bonding in all the independent simulations (Fig. S31 in Appendix A), along with the binding between the Thr6 and Asn8 and the ice. A detailed analysis of these hydrogen bonding interactions suggested that they mainly occurred after 20 ns (Fig. S32 in Appendix A). Therefore, a mutant termed AVD-5 that lacked the normal amide bond between Ser18 and Gly19 was designed by inserting aminohexanoic acid (Ahx) into this position (Fig. 4(a)). MS and HPLC data for the mutant AVD-5 are provided in Fig. S33 in Appendix A. The antifreeze properties of the mutant were investigated. As shown in Figs. 4(b) and (d), AVD-5 displayed a higher ice growth rate than AVD. In addition, AVD-5 lost most of its IRI activity, similar to the mutant AVD-2 (Figs. 4(c) and (e)), which further indicated the supporting role of residue Ser18. This supplemental interaction may synergistically stabilize the binding of the AVD peptide with ice and hinder the ice growth.

3.5. Cell cryopreservation with AVD

Cell-based therapy and diagnosis are desirable for supporting human health, and the cells used for such purposes generally need to be cryopreserved for clinical applications [37–40]. Herein, AVD was employed as a novel CPA for cell cryopreservation. First, cytotoxicity, hemocompatibility, and immunogenicity tests were conducted to evaluate the biocompatibility of AVD. Three different cell lines containing fibroblast NIH-3T3, macrophage RAW264.7, and lung adenocarcinoma cell GLC-82 were cultured separately with different concentrations of AVD. As shown in Fig. S34(a) in Appendix A, no difference was observed between the experimental and the control groups for each cell line. In addition, the caspase signaling pathway of RAW264.7 was detected to evaluate the cytocompatibility. The transcript levels of caspases 3, 4, 8, and 9 exhibited insignificant differences in all samples (Fig. S34(b) in Appendix A), indicating the cytocompatibility of AVD. Moreover, in the hemocompatibility test, the hemolysis rates (HRs) of all AVD samples were found to be less than 0.8%, satisfying the clinical requirement (HR < 5%) (Figs. S34(c) and (d) in Appendix A). The immunogenicity was also investigated by determining the transcript levels of pro- and anti-inflammatory markers, including TNF-α, CD163, IL-1, iNOS, VEGF, CD206, Arg-1, and IL-10. The relative messenger RNA (mRNA) levels of the markers were similar in both the control and AVD groups, revealing negligible immunogenicity (Fig. S34(e) in Appendix A).

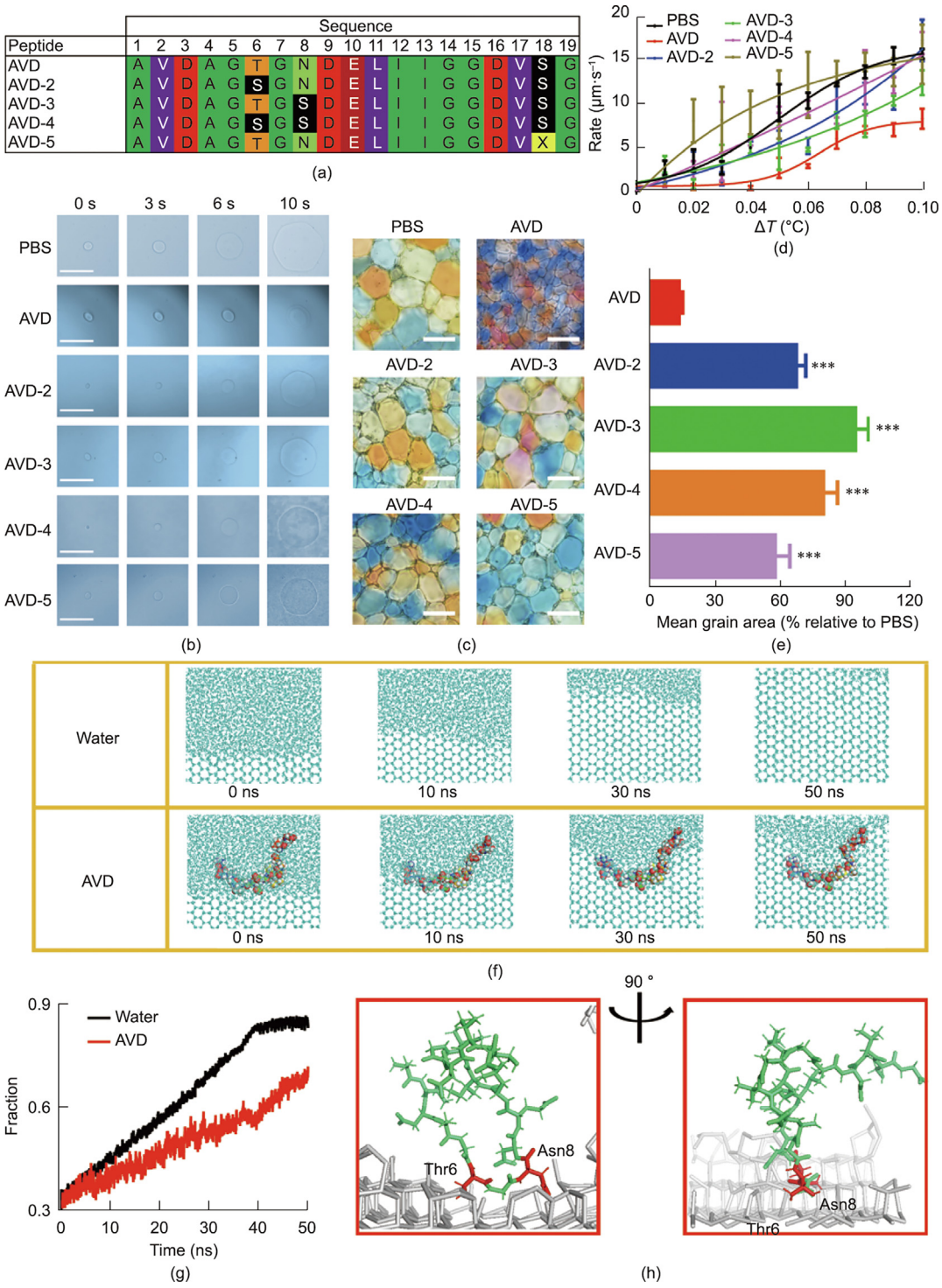

Fig. 4. Mutational analysis and MD simulations of the AVD peptide. (a) Sequences of AVD and its mutants. X indicates that the carboxyl group of Ser was replaced by aminohexanoic acid (Ahx). (b) Single ice crystals grown in solutions of AVD and its mutants (scale bar: 100 μm). (c) Representative cryomicrographs of ice crystals grown in the presence of AVD and its mutants (scale bar: 100 μm). (d) Ice growth rates in solutions of different peptides. (e) Quantitative analysis of IRI activities for different peptides. (f) Snapshots of ice growth in the control and AVD solutions during the MD simulations. (g) Ice fraction data in water and the AVD solutions during the MD simulations. (h) Snapshots of AVD binding to ice from two different perspectives (Thr6 and Asn8 of AVD are colored red, other residues are green, and ice crystals are shown in gray).

The excellent IRI and biocompatibility properties of the AVD peptide pave the way for cell cryopreservation. Here, both AVD and the negative control AVD-3 peptide were employed. Three cell lines including NIH-3T3, RAW264.7, and GLC-82 were selected. Cell recoveries were detected at 24 h post thawing to enable apoptotic events to occur and avoid false-positive results [41]. Higher cell recovery was obtained with increased AVD concentrations. Cell recoveries of 70.9%, 34.9%, and 95.7% were achieved for NIH-3T3, RAW264.7, and GLC-82 with 10 mg·mL^{-1} AVD as a CPA—recoveries that were 2.5, 14.5, and 3.1 times higher, respectively, than those without AVD (Figs. 5(a)–(c)). These recovery rates were also 2.6, 1.8, and 1.3 times higher than

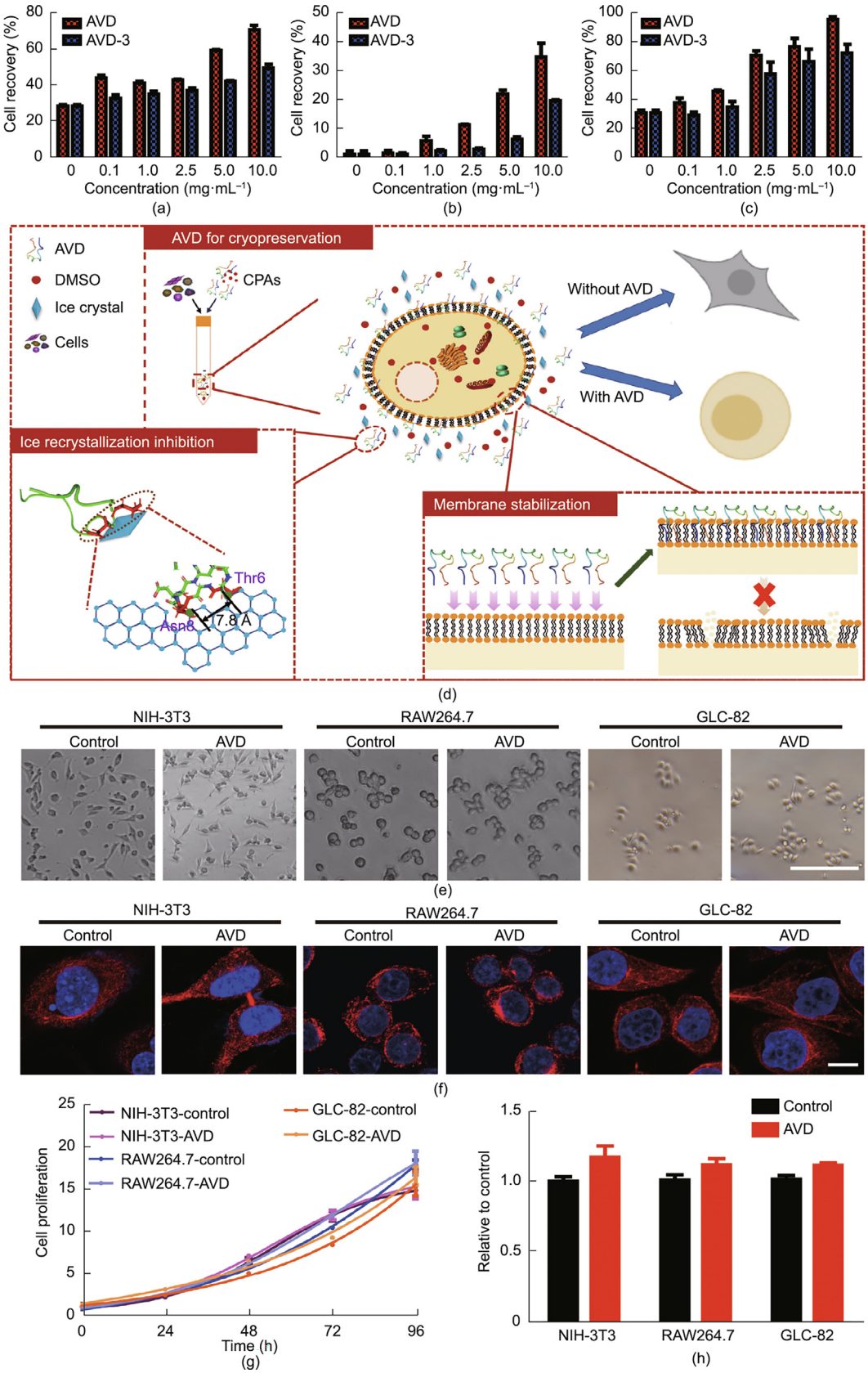

Fig. 5. (a–c) The post-thaw cell recovery of (a) NIH-3T3, (b) RAW264.7, and (c) GLC-82 cells. The post-thaw cell recovery was calculated with a Trypan blue exclusion assay. (d) Schematics of the mechanism of AVD for cell cryopreservation. (e) Cell morphology of post-thawed NIH-3T3, RAW264.7, and GLC-82 cells (scale bar: 100 μm). (f) Immunofluorescence photographs of tubulin morphology and the chromosome alignment of post-thawed NIH-3T3, RAW264.7, and GLC-82 cells (red color: α-tubulin-FITC staining; blue color: Hoechst 33342 staining of the chromosome; merge: merge of α-tubulin-FITC staining and Hoechst 33342 staining images; scale bar: 10 μm). (g) Proliferation curves of post-thawed cells of NIH-3T3, RAW264.7, and GLC-82. (h) ATP level in post-thawed cells. The AVD concentration is 10 mg·mL^{-1} for experiments (e–h).

those of the AVD-3 peptide, indicating that AVD is an effective CPA component (Figs. 5(a)–(c)).

The cryopreservation effect of the peptides prompted us to investigate other potential mechanisms, as IRI may not be the only factor for the cryopreservation abilities of antifreeze materials [42,43]. We employed a live/dead assay to explore the post-thaw membrane permeation [44,45]. As shown in Fig. S35 in Appendix A, the cells that were cryopreserved without peptides exhibited a significant amount of damaged membrane post-thaw, resulting in more red nuclei. In contrast, the proportion of cells with damaged membranes was significantly decreased with the addition of the AVD and AVD-3 peptides, indicating that these peptides can stabilize the cell membranes during freeze/thaw cycles.

FITC-labeled AVD was further employed to investigate the role of AVD in protecting cell membranes. Fluorescence appeared on the cell membranes after the cells were cultured with FITC-labeled AVD, while fluorescence was observed all over the cells after incubated only with FITC molecules, indicating that AVD interacts with the cell membranes (Fig. S36(a) in Appendix A). The cell membrane potential—a sensitive index to determine the functional integrity of membranes—was also examined with lipophilic anionic fluorescent dye D43 [46]. After stored at 4 °C for 48 h, cells incubated with AVD displayed a fluorescence strength similar to that of fresh cells, while the control sample without AVD showed much stronger fluorescence, indicating depolarization and damage of the cell membrane (Figs. S36(b) and (c) in Appendix A).

Blocking the Ca^{2+} pumps can balance the ion composition and prevent membrane damage during cryopreservation [47]. Therefore, the Ca^{2+} permeability in the cell membranes was investigated by monitoring the change in the fluorescence ratio (R340/380) (Fig. S36(d) in Appendix A). The ratio of R340/380 increased significantly in the control group after Ca^{2+} treatment, while little change was observed in the AVD group. Correspondingly, a rapid and strong shift from red to green was observed in the control group, whereas the color change seemed to be moderate and stable in the AVD group (Fig. S36(e) in Appendix A). Moreover, a higher fluorescence ratio was observed in the control group, while a steady trend was obtained in the AVD group with an increase in Ca^{2+} concentration (Fig. S37 in Appendix A). These results demonstrate that AVD can retain the integrity of the cell membrane by balancing the ion compositions during cryopreservation. Overall, AVD can cryopreserve cells by synergistically inhibiting ice recrystallization and stabilizing the cell membrane during thawing/melting (Fig. 5(d)).

It is also important to investigate whether cells are really viable after freezing–thawing. Here, the cell attachment and proliferation were evaluated. As shown in Figs. 5(e) and (f), similar to the fresh cells, the post-thawed cells were still able to attach to the substrate, and there were obvious actin-dependent protrusions and cytoplasmic projections, indicating that AVD could sustain the cellular ultrastructure. Furthermore, the post-thawed cells possessed similar proliferation rates compared with fresh cells, demonstrating their normal viability and cellular metabolism (Fig. 5(g)). The post-thawed cells also possessed similar ATP levels compared with fresh cells (Fig. 5(h)), demonstrating the integrity of their mitochondria which can be easily damaged during the freeze–thawing process [48]. The cell cryopreservation efficiency of AVD and other reported IBPs or IBP mimics are summarized in Table S7 in Appendix A. Overall, these results demonstrate that AVD can be employed as a novel and effective CPA that maintains cell functionality after freeze–thawing cycles. Finally, it should be noted that ice recrystallization is particularly serious during the warming process of vitrification [49]. Therefore, vitrification will be employed for cell cryopreservation with AVD as a CPA in our future work.

4. Conclusions

Repetitive motifs in various IBPs were successfully employed to design efficient antifreeze peptides through systematic classification and evolutionary analysis. After comprehensively considering the samples' solubilities and IRI activities, the optimally designed AVD peptide was selected for further study in more detail. Based on a combination of mutation analysis and MD simulations, it was concluded that the Thr6 and Asn8 residues of the AVD peptide are essential to its ability to bind to ice, while the Ser18 residue can further stabilize the peptide's interactions with ice through hydrogen bonding. In addition, AVD exhibited excellent biocompatibility and could interact with and stabilize cell membranes by blocking calcium ion channels. With these advantages, the AVD peptide was successfully employed as a CPA and significantly increased the post-freezing cell recovery. The strategy proposed in this work can be used to design novel antifreeze peptides; it will also enrich the module library of synthetic biology and is expected to have a significant impact on the field of cell and tissue cryopreservation.

Acknowledgments

This research was financially supported by the National Key Research and Development Program of China (2021YFC2100800); the National Natural Science Foundation of China (22078238, 21961132005, and 21908160); the Open Funding Project of the National Key Laboratory of Biochemical Engineering; and the Program of Introducing Talents of Discipline to Universities (BP0618007).

Compliance with ethics guidelines

Haishan Qi, Yihang Gao, Lin Zhang, Zhongxin Cui, Xiaojie Sui, Jianfan Ma, Jing Yang, Zhiquan Shu, and Lei Zhang declare that they have no conflict of interest or financial conflicts to disclose.

Appendix A. Supplementary data

Supplementary data to this article can be found online at https://doi.org/10.1016/j.eng.2023.01.015.

References

[1] Bar Dolev M, Braslavsky I, Davies PL. Ice-binding proteins and their function. Annu Rev Biochem 2016;85(1):515–42.
[2] Liu K, Wang C, Ma J, Shi G, Yao X, Fang H, et al. Janus effect of antifreeze proteins on ice nucleation. Proc Natl Acad Sci USA 2016;113(51):14739–44.
[3] Wu J, Rong Y, Wang Z, Zhou Y, Wang S, Zhao B. Isolation and characterisation of sericin antifreeze peptides and molecular dynamics modelling of their ice-binding interaction. Food Chem 2015;174:621–9.
[4] Bai G, Gao D, Liu Z, Zhou X, Wang J. Probing the critical nucleus size for ice formation with graphene oxide nanosheets. Nature 2019;576(7787):437–41.
[5] Liu Z, Zheng X, Wang J. Bioinspired ice-binding materials for tissue and organ cryopreservation. J Am Chem Soc 2022;144(13):5685–701.
[6] Stevens CA, Bachtiger F, Kong XD, Abriata LA, Sosso GC, Gibson MI, et al. A minimalistic cyclic ice-binding peptide from phage display. Nat Commun 2021;12(1):2675.
[7] Marcotte EM, Pellegrini M, Yeates TO, Eisenberg D. A census of protein repeats. J Mol Biol 1999;293(1):151–60.
[8] Levinson G, Gutman GA. Slipped-strand mispairing: a major mechanism for DNA sequence evolution. Mol Biol Evol 1987;4(3):203–21.
[9] Charlesworth B, Sniegowski P, Stephan W. The evolutionary dynamics of repetitive DNA in eukaryotes. Nature 1994;371(6494):215–20.
[10] Basu K, Campbell RL, Guo S, Sun T, Davies PL. Modeling repetitive, non-globular proteins. Protein Sci 2016;25(5):946–58.
[11] DeVries AL, Wohlschlag DE. Freezing resistance in some Antarctic fishes. Science 1969;163(3871):1073–5.
[12] Mularoni L, Ledda A, Toll-Riera M, Albà MM. Natural selection drives the accumulation of amino acid tandem repeats in human proteins. Genome Res 2010;20(6):745–54.

[13] Lutz S. Beyond directed evolution—semi-rational protein engineering and design. Curr Opin Biotechnol 2010;21(6):734–43.
[14] Liu LQ, Liu H, Zhang W, Yao MD, Li BZ, Liu D, et al. Engineering the biosynthesis of caffeic acid in *Saccharomyces cerevisiae* with heterologous enzyme combinations. Engineering 2019;5(2):287–95.
[15] Bednar D, Beerens K, Sebestova E, Bendl J, Khare S, Chaloupkova R, et al. FireProt: energy- and evolution-based computational design of thermostable multiple-point mutants. PLOS Comput Biol 2015;11(11):e1004556.
[16] Ma Y, Yao MD, Li BZ, Ding MZ, He B, Chen S, et al. Enhanced poly(ethylene terephthalate) hydrolase activity by protein engineering. Engineering 2018;4(6):888–93.
[17] Swanson WJ, Aquadro CF. Positive Darwinian selection promotes heterogeneity among members of the antifreeze protein multigene family. J Mol Evol 2002;54(3):403–10.
[18] Abascal JLF, Sanz E, García Fernández R, Vega C. A potential model for the study of ices and amorphous water: TIP4P/Ice. J Chem Phys 2005;122(23):234511.
[19] Murray KA, Gibson MI. Post-thaw culture and measurement of total cell recovery is crucial in the evaluation of new macromolecular cryoprotectants. Biomacromolecules 2020;21(7):2864–73.
[20] Liou YC, Tocilj A, Davies PL, Jia Z. Mimicry of ice structure by surface hydroxyls and water of a β-helix antifreeze protein. Nature 2000;406(6793):322–4.
[21] Graether SP, Kuiper MJ, Gagné SM, Walker VK, Jia Z, Sykes BD, et al. β-Helix structure and ice-binding properties of a hyperactive antifreeze protein from an insect. Nature 2000;406(6793):325–8.
[22] Garnham CP, Gilbert JA, Hartman CP, Campbell RL, Laybourn-Parry J, Davies PL. A Ca^{2+}-dependent bacterial antifreeze protein domain has a novel β-helical ice-binding fold. Biochem J 2008;411(1):171–80.
[23] Zhang DQ, Liu B, Feng DR, He YM, Wang SQ, Wang HB, et al. Significance of conservative asparagine residues in the thermal hysteresis activity of carrot antifreeze protein. Biochem J 2004;377(3):589–95.
[24] John UP, Polotnianka RM, Sivakumaran KA, Chew O, Mackin L, Kuiper MJ, et al. Ice recrystallization inhibition proteins (IRIPs) and freeze tolerance in the cryophilic Antarctic hair grass *Deschampsia antarctica* E. Desv. Plant Cell Environ 2009;32(4):336–48.
[25] Zimmermann L, Stephens A, Nam SZ, Rau D, Kübler J, Lozajic M, et al. A completely reimplemented MPI bioinformatics toolkit with a new HHpred server at its core. J Mol Biol 2018;430(15):2237–43.
[26] Biegert A, Söding J. *De novo* identification of highly diverged protein repeats by probabilistic consistency. Bioinformatics 2008;24(6):807–14.
[27] Gabler F, Nam SZ, Till S, Mirdita M, Steinegger M, Söding J, et al. Protein sequence analysis using the MPI bioinformatics toolkit. Curr Protoc Bioinformatics 2020;72(1):e108.
[28] Bayer-Giraldi M, Weikusat I, Besir H, Dieckmann G. Characterization of an antifreeze protein from the polar diatom *Fragilariopsis cylindrus* and its relevance in sea ice. Cryobiology 2011;63(3):210–9.
[29] Arai T, Fukami D, Hoshino T, Kondo H, Tsuda S. Ice-binding proteins from the fungus *Antarctomyces psychrotrophicus* possibly originate from two different bacteria through horizontal gene transfer. FEBS J 2019;286(5):946–62.
[30] Bailey TL, Elkan C. Fitting a mixture model by expectation maximization to discover motifs in biopolymers. Proc Int Conf Intell Syst Mol Biol 1994;2:28–36.
[31] Congdon T, Notman R, Gibson MI. Antifreeze (glyco)protein mimetic behavior of poly(vinyl alcohol): detailed structure ice recrystallization inhibition activity study. Biomacromolecules 2013;14(5):1578–86.
[32] Graham B, Fayter AER, Gibson MI. Synthesis of anthracene conjugates of truncated antifreeze protein sequences: effect of the end group and photocontrolled dimerization on ice recrystallization inhibition activity. Biomacromolecules 2019;20(12):4611–21.
[33] Geng H, Liu X, Shi G, Bai G, Ma J, Chen J, et al. Graphene oxide restricts growth and recrystallization of ice crystals. Angew Chem Int Ed Engl 2017;56(4):997–1001.
[34] Garnham CP, Campbell RL, Davies PL. Anchored clathrate waters bind antifreeze proteins to ice. Proc Natl Acad Sci USA 2011;108(18):7363–7.
[35] Hudait A, Qiu Y, Odendahl N, Molinero V. Hydrogen-bonding and hydrophobic groups contribute equally to the binding of hyperactive antifreeze and ice-nucleating proteins to ice. J Am Chem Soc 2019;141(19):7887–98.
[36] Chao H, Houston Jr ME, Hodges RS, Kay CM, Sykes BD, Loewen MC, et al. A diminished role for hydrogen bonds in antifreeze protein binding to ice. Biochemistry 1997;36(48):14652–60.
[37] Gao JM, Yu XY, Wang XL, He YN, Ding JD. Biomaterial-related cell microenvironment in tissue engineering and regenerative medicine. Engineering 2022;13:31–45.
[38] Blazar BR. Immune regulatory cell biology and clinical applications to prevent or treat acute graft-versus-host disease. Engineering 2019;5(1):98–105.
[39] Li YH, Huo Y, Yu L, Wang JZ. Quality control and nonclinical research on CAR-T cell products: general principles and key issues. Engineering 2019;5(1):122–31.
[40] Horiguchi I, Kino-oka M. Current developments in the stable production of human induced pluripotent stem cells. Engineering 2021;7(2):144–52.
[41] Tomás RMF, Bissoyi A, Congdon TR, Gibson MI. Assay-ready cryopreserved cell monolayers enabled by macromolecular cryoprotectants. Biomacromolecules 2022;23(9):3948–59.
[42] Bailey TL, Stubbs C, Murray K, Tomás RMF, Otten L, Gibson MI. Synthetically scalable poly(ampholyte) which dramatically enhances cellular cryopreservation. Biomacromolecules 2019;20(8):3104–14.
[43] Sun Y, Maltseva D, Liu J, Hooker II T, Mailänder V, Ramløv H, et al. Ice recrystallization inhibition is insufficient to explain cryopreservation abilities of antifreeze proteins. Biomacromolecules 2022;23(3):1214–20.
[44] Bratosin D, Mitrofan L, Palii C, Estaquier J, Montreuil J. Novel fluorescence assay using calcein-AM for the determination of human erythrocyte viability and aging. Cytom Part A 2005;66A(1):78–84.
[45] Galluzzi L, Aaronson SA, Abrams J, Alnemri ES, Andrews DW, Baehrecke EH, et al. Guidelines for the use and interpretation of assays for monitoring cell death in higher eukaryotes. Cell Death Differ 2009;16(8):1093–107.
[46] Rubinsky B, Arav A, Mattioli M, Devries AL. The effect of antifreeze glycopeptides on membrane potential changes at hypothermic temperatures. Biochem Biophys Res Commun 1990;173(3):1369–74.
[47] Rubinsky B, Mattioli M, Arav A, Barboni B, Fletcher GL. Inhibition of Ca^{2+} and K^{+} currents by "antifreeze" proteins. Am J Physiol 1992;262(3 Pt 2):R542–5.
[48] Yamaguchi R, Andreyev A, Murphy AN, Perkins GA, Ellisman MH, Newmeyer DD. Mitochondria frozen with trehalose retain a number of biological functions and preserve outer membrane integrity. Cell Death Differ 2007;14(3):616–24.
[49] Huang H, Zhao G, Zhang Y, Xu J, Toth TL, He X. Predehydration and ice seeding in the presence of trehalose enable cell cryopreservation. ACS Biomater Sci Eng 2017;3(8):1758–68.